High-Efficacy Hierarchical Dy$_2$O$_3$/TiO$_2$ Nanoflower toward Wastewater Reclamation: A Combined Photoelectrochemical and Photocatalytic Strategy

Mahmoud M. Kaid, Abdelrahman S. Khder,* Saleh A. Ahmed,* Amr A. Ibrahim, Hatem M. Altass, Reem I. Alsantali, Rabab S. Jassas, Menna A. Khder, Munirah M. Al-Rooqi, Ziad Moussa, and Awad I. Ahmed*

Cite This: *ACS Omega* 2022, 7, 17223−17233

Read Online

ACCESS | Metrics & More | Article Recommendations | SI Supporting Information

ABSTRACT: Developing a sustainable photocatalyst is crucial to mitigate the foreseeable energy shortage and environmental pollution caused by the rapid advancement of global industry. We developed Dy$_2$O$_3$/TiO$_2$ nanoflower (TNF) with a hierarchical nanoflower structure and a near-ideal anatase crystallite morphology to degrade aqueous rhodamine B solution under simulated solar light irradiation. The prepared photocatalyst was well-characterized using powder X-ray diffraction, Fourier transform infrared spectroscopy, transmission electron microscopy, energy-dispersive spectroscopy, scanning electron microscopy, Brunauer-Emmett-Teller, diffuse reflectance UV-vis spectra, and X-ray photoelectron spectroscopy. Further analysis was performed to highlight the photoelectrochemical activity of the prepared photocatalysts such as electrochemical impedance spectroscopy, linear sweep voltammetry, photocurrent response, and a Mott−Schottky study. The crystalline Dy$_2$O$_3$/TNF exhibits superb photocatalytic activity attributed to the improved charge transfer, reduced recombination rate of the electron−hole pairs, and a remarkable red-shift in light absorption.
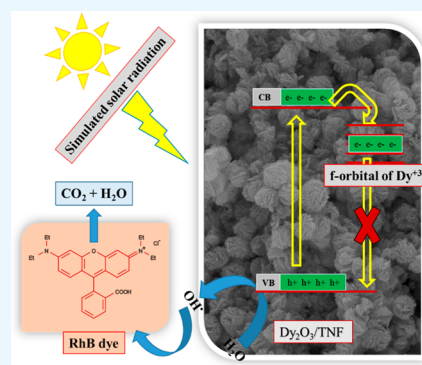
1. INTRODUCTION

Synthetic dyes present in wastewater pose a significant hazard to the health of both the ecosystem and humans. The total production of synthetic dyes used in the industry to color plastics, leather, fabric, cosmetics, foodstuffs, and other consumer products is ∼7 × 10^5 tons per annum. The rating indicates that 2−10% of the produced dyes are ultimately discharged as effluent wastes into rivers and streams.[1−6] Advanced Oxidation Processes (AOPs) are a developed wastewater treatment, which generates highly reactive radicals (·OH, ·O$_2^-$, and so on) using photocatalysts to oxidize O$_2$ and H$_2$O molecules by irradiation with UV−vis light. These radicals interact with organic pollutants and convert them to nontoxic small molecules (H$_2$O and CO$_2$). However, the main challenge facing AOPs since Glaze et al. formally defined the concept in 1987 is the high ultraviolet (UV) light required as energy input to produce the highly active radicals.[1,7,8] Therefore, finding a catalyst to lower the efficient activation energy is the basis of the next-generation AOPS. Previous studies have focused mainly on an activation energy strategy through the single-electron redox cycle of the exposed transition metals such as Cu,[9] Fe,[10] and Mn,[11] on various supports (activated carbon, zeolites, and magnetite). Fenton's reagent as an example of a homogeneous catalyst suffers from

drawbacks, including the recyclability of Fe^{2+}, the requirement of a very low pH medium, and the accumulation of iron-containing sludge.[9−12]

Recently, semiconductor photocatalysis has emerged as an important solution to energy scarcity and environmental protection. The materials' bandgap energy, specific surface area, morphology, and conductivity are the critical factors for the photocatalytic property.[13−18] Irradiation of photocatalysts produces holes in the valence band (VB) and electrons in the conduction band. Holes undergo an oxidation reaction to generate hydroxyl radicals (·OH), while electrons react with oxygen in the air through a reduction process to produce superoxide radical anions (·O$_2^-$). The organic pollutants can be degraded by these active radicals to create H$_2$O and CO$_2$.[19−21] Several strategies have been studied to enhance the photocatalytic efficiency of visible-light photocatalysts, in particular, doping, band gap regulation, structural control,

surface sensitization, and phase transfer.[22−24] Characteristic features of efficient photocatalysts include photoactivity to biological and chemical matters, nontoxicity, ability to absorb near UV−visible regions, photostability, and cost-effectiveness.

TiO$_2$ photocatalyst is widely used for photo-oxidation of organic pollutants. The valence and conduction band of TiO$_2$ anatase is at +2.7 and −0.5 eV versus standard hydrogen electrode (SHE), respectively.[2−5] The solar energy spectrum consists of only 5−7% ultraviolet (UV), 47% infrared (IR), and 46% visible radiation.[25,26] Although TiO$_2$ is active in the UV region, developing a novel TiO$_2$-based photocatalyst with an improved band gap has gained importance for advancing visible-light photocatalysis. Recently, pure anatase nanorods were synthesized by a thermal treatment of H$_3$Ti$_3$O$_7$ nanotubes at 700 °C and showed superior performance with regard to dye degradation by comparison with Evonik P25 TiO$_2$ (15% rutile + 85% anatase), reflecting the role of morphology in the photocatalyst performance.[27−29] Lui et al. studied the photocatalytic efficiency of graphene-wrapped TiO$_2$ nanoflowers (TNFs) with 5 wt % graphene loading for methylene blue (MB) solution degradation, and the results outperformed P25 TiO$_2$ by threefold.[29] Harris et al. investigated the efficiency of a series of TiO$_2$ nanoflowers as a catalyst for the photo-oxidation of MB with remarkable activity under UV irradiation.[2] Various morphologies of TiO$_2$ have been studied extensively as a photocatalyst for the degradation of organic pollutants, including nano- and microparticles, nanowires, nanotubes, and hierarchical morphologies.[27,30,31] The later morphology is of great interest due to their ability to combine the high surface area of small particles (increase the material's capacity for adsorption) with the light-scattering ability of the larger particles (increase the probability of photon absorption).[2,29] Liao et al. synthesized a flower-like morphology as an example of hierarchical materials with a relatively large surface area, large size, and enhanced charge transfer for use in dye-sensitized solar cells.[32]

Although lanthanide materials are familiar insulators, incorporating semiconductors with lanthanides enhanced the photocatalytic performance of the material due to the presence of f-orbitals that trap the photogenerated electrons on irradiation with other semiconductors.[25,33] The doping of ZnO with a lanthanide material has been recently studied by Josephine et al. as a photocatalyst under visible-light radiation.[33] The synthesized Dy$_2$O$_3$@SiO$_2$@ZnO was investigated as a highly visible active photocatalyst for degradation of the endocrine disruptor 2,4-D.[25] Sheydaei et al. studied the photocatalytic ozonation of wastewater via the immobilization of TiO$_2$, graphite, and Dy$_2$O$_3$ and achieved 90% decolorization efficiency.[34]

Herein we present Dy$_2$O$_3$/TNF as a wastewater treatment photocatalyst that successfully tackles the aforementioned challenges regarding current AOPs. This photocatalyst is enabled by incorporating Dy$_2$O$_3$ with TNF to solve the current photocatalysts' challenges and exhibits superior activity to generate ·O$_2^-$ and ·OH radicals at pH 8. The specific aims of the present study are (1) a hydrothermal synthesis of TiO$_2$ nanoflower, (2) modification of TNF via doping with Dy$_2$O$_3$ and calcination at 700 °C, (3) detailed physicochemical and photoelectrochemical characterization of the synthesized Dy$_2$O$_3$/TNF, and (4) investigate the photocatalytic efficiency of Dy$_2$O$_3$/TNF for wastewater treatment. To fully understand the photocatalytic degradation process, the effects of solution pH, initial dye concentration, adsorbent dosage, and contact time on the photodegradation of RhB dye under simulated solar light irradiation were successfully studied.

2. EXPERIMENTAL SECTION

2.1. Chemicals. Titanium butoxide, dysprosium(III) nitrate pentahydrate, glacial acetic acid, absolute ethanol, HCl, NaOH, and rhodamine B (RhB) dye were all obtained from Sigma-Aldrich and used without further treatment.

2.2. Synthesis of TiO$_2$ and Dy$_2$O$_3$/TiO$_2$ Nanoflower. TNFs were hydrothermally synthesized based on a typical procedure reported by Harris et al.[2] Briefly, 2 mL of titanium butoxide was slowly added and stirred vigorously with 60 mL of glacial acetic acid at room temperature. After 15 min, the white suspension was placed in a 100 mL Teflon-lined autoclave and transferred into a preheated oven at 140 °C for 12 h. The resultant white product was separated by centrifugation (7000 rpm, 5 min) and washed several times by deionized water. Then the solvent was exchanged by ethanol (total amount 100 mL), and the obtained product was dried overnight at 60 °C. The dried powder was placed in a crucible and calcined in a muffle furnace for 3 h at 700 °C with a heating rate of 5 °C/min. In order to prepare Dy$_2$O$_4$/TiO$_2$ nanoflower samples, the same previous steps were followed, except for adding specific amounts of a certain amount of Dy(NO)$_3$·5H$_2$O to finally obtain (1−10%) of Dy$_2$O$_3$/TiO$_2$ nanoflowers after burning at 700 °C for 2 h.

2.3. Characterization. The as-synthesized photocatalysts were characterized by Fourier transform infrared (FT-IR) recorded on a Mattson FT-IR-5000S spectrophotometer using a KBr pellet with 4 cm^{-1} resolution. X-ray diffraction (XRD) patterns were implemented at a scanning rate of 2°·min^{-1} using monochromatic Cu Kα radiation (40 kV, 40 mA). Rutile (R) and anatase (A) crystallite sizes (l) were investigated by the Scherrer equation depending on the main reflection peak of rutile (110) and anatase (101) at 2θ = 27.3 and 24.9°, respectively. The rutile phase ratio (%R) in the prepared catalysts was determined using the following equation[2]

$$\%R = \frac{1}{\left[1 + 0.8\left(\frac{I_A}{I_R}\right)\right]} \times 100$$

(1)

where I_A and I_R are the peak intensities for the rutile and anatase reflections, respectively. The surface compositions and the oxidation state of the catalysts were analyzed by the X-ray photoelectron spectroscopy (XPS) technique. The analyses used a Kratos Axis Ultra DLD equipped with a monochromatic Al Kα X-ray source (1486.69 eV) and a hemispherical electron energy analyzer. Survey scans were acquired at a pass energy of 80 eV, and core-level scans were acquired at a pass energy of 20 eV. For binding energy scale calibration, adventitious hydrocarbon referencing (C 1s signal at 285.0 eV) was used. The morphology of prepared materials was studied by using transmission electron microscopy (TEM), a JEOL-JEM-2100 instrument with a slow-scan charge-coupled device (CCD), which was operated at 120 kV, and scanning electron microscopy (SEM, JEOL-JSM-6510 LV) at 5−10 kV. A nitrogen adsorption study over the prepared catalysts was performed at −196 °C using QuantaChrome NOVA touch LX^4 equipment. Before the measurement, the catalysts were activated at 300 °C for 3 h under vacuum. Diffuse reflectance spectra (UV−vis−NIR (NIR = near-infrared)) referenced to BaSO$_4$ were obtained using a Fischer Scientific spectrometer
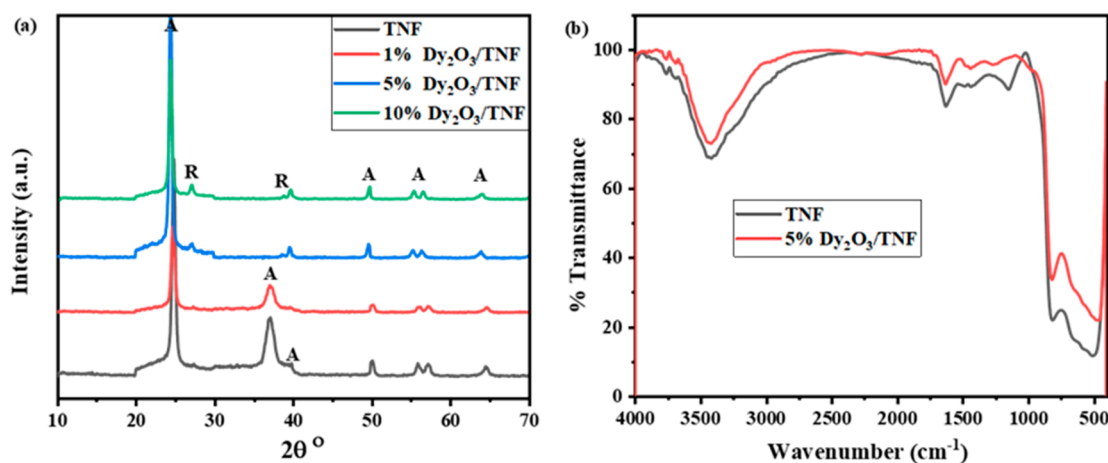
Figure 1. (a) XRD and (b) FT-IR of some selected samples calcined at 700 °C.

EVO 300. The band gaps of TNF and Dy_2O_3/TNF composites were directly calculated by a Tauc plot applying the Kubelka−Munk function.[2]

2.4. Electrochemical Measurements. Photoelectrochemical measurements were obtained at room temperature in a 0.5 M Na_2SO_4 solution using a three-electrode configuration CHI 6005E (CH Instruments) Electrochemical Analyzer. TNF and Dy_2O_3/TNF samples were completely covered with a fluorine-doped tin oxide (FTO) sheet and used as the working electrode. Ag/AgCl (KCl, saturated) and a Pt sheet were used as reference and counter electrodes, respectively. The photocatalyst sample was well-dispersed in a 1 mL-sized tube under sonication with 450 μL of absolute ethanol and 50 μL of 5 wt % Nafion solution. After sonication for 1 h, a 10 μL suspension was dropped over a well-cleaned FTO sheet based on the experiment type and thoroughly dried at room temperature. The photocurrent response intensity of TNF and Dy_2O_3/TNF composites was completely distinct for several intermittent switching turning to light. The photocurrent density ($J-\nu$ curves) and linear sweep voltammetry (LSV) test that provide the background capacitive current of the synthesized materials were displayed under 1 Sun illumination (AM 1.5G) in a 0.5 M Na_2SO_4 aqueous solution. Electrochemical impedance spectroscopy (EIS) measurements were conducted in a frequency range between 0.1 Hz and 100 kHz at 298 K in a 250 mL cell containing 0.1 M KOH as electrolytic solution saturated with N_2 for 15 min to remove other dissolved gas. Mott−Schottky (MS) measurements were utilized to investigate the band edge potential of the absolute semiconductor components and the type of semiconductivity. The Applied Bias Photon to current conversion Efficiency (% of ABPE) was estimated using eq 2.[36]

$$\eta(\%) = \frac{J_{ph} \times (1.23 - |E_{RHE}|)}{P_{total}} \times 100 \quad (2)$$

Here, η and J_{ph} are the efficiency and the obtained photocurrent density, respectively. P_{total} is the total incident power density (100 mW/cm²), and E_{RHE} is the applied bias versus reversible hydrogen electrode and calculated using eq 3.

$$E_{RHE} = E_{Ag/AgCl} + E^0_{Ag/AgCl} + 0.059pH \quad (3)$$

The standard potential of Ag/AgCl as a reference electrode, $E^0_{Ag/AgCl}$, equals 0.1976 V at 25 °C. The following Mott−

Schottky equation was used to obtain the charge carrier density[37,38]

$$\frac{1}{C^2} = \frac{2}{N_D e \varepsilon \varepsilon_o}\left[(V_s - E_{FB}) - \frac{k_B T}{e}\right] \quad (4)$$

where C is the space charge capacitance, e is an elemental charge, N_D is the electron carrier density, ε is the relative permittivity of semiconductor, ε_o is the permittivity of vacuum, k_B is the Boltzmann constant, T is the absolute temperature, V_s is the applied potential, and E_{FB} is flat band potential. Herein, $k_B = 1.380\,648\,52 \times 10^{-23}$ m² kg s⁻² K⁻¹, e = -1.6×10^{-19} C, $\varepsilon_0 = 8.854 \times 10^{-12}$ F m⁻¹, and $\varepsilon = 7.7$ for TNF.[39,40]

2.5. Photocatalytic Activity. The whole photocatalytic process was performed by transferring 20 mg of the photocatalyst to 50 mL of RhB dye solution in a reaction quartz tube and irradiating it using (SciSun-300) Solar Simulator, Class AAA, 300 W, 50 × 50 mm, (100 mW/cm²) equipped with an AM 1.5G filter. The catalyst−dye mixture was first stirred by a magnetic stirrer in the dark for 1 h to attain adsorption−desorption equilibrium. After that, the xenon lamp was turned on, and the photocatalytic degradation of the RhB dye was studied for 2 h. At regular time intervals, 0.5 mL of the sample was taken out and diluted to 5 mL with distilled water, then centrifuged to remove the catalyst powder. The absorbance of the 2 mL centrifuged solution was acquired using a UV−vis spectrophotometer at 554 nm to investigate the remaining concentrations of RhB dye.

3. RESULTS AND DISCUSSION

The powder XRD pattern was used to investigate the polymorph phases of TiO_2 that exist in the TNF photocatalysts, and the results are displayed in Figure 1. According to Figure 1a, pure TNF shows well-defined and intense diffraction peaks at 2θ = 24.9, 37.1, 39.8, 49.8, and 55.5°, which are typical for the anatase phase.[40,41] Moreover, doping of Dy_2O_3 into TNF results in the appearance of new weak diffraction peaks at 2θ = 27.3 and 38.8° that are assigned to the rutile phase. Considering these results, calcination of TiO_2 at 700 °C yielded TNF that was ∼100% anatase phase, while annealing with Dy_2O_3 results in TNF composites that consist of predominant anatase (>95%) and minority rutile (<5%) phases. The presence of Dy_2O_3 induces the rutile crystallite growth and preserves the anatase as the main phase with important implications for the photocatalytic performance, as
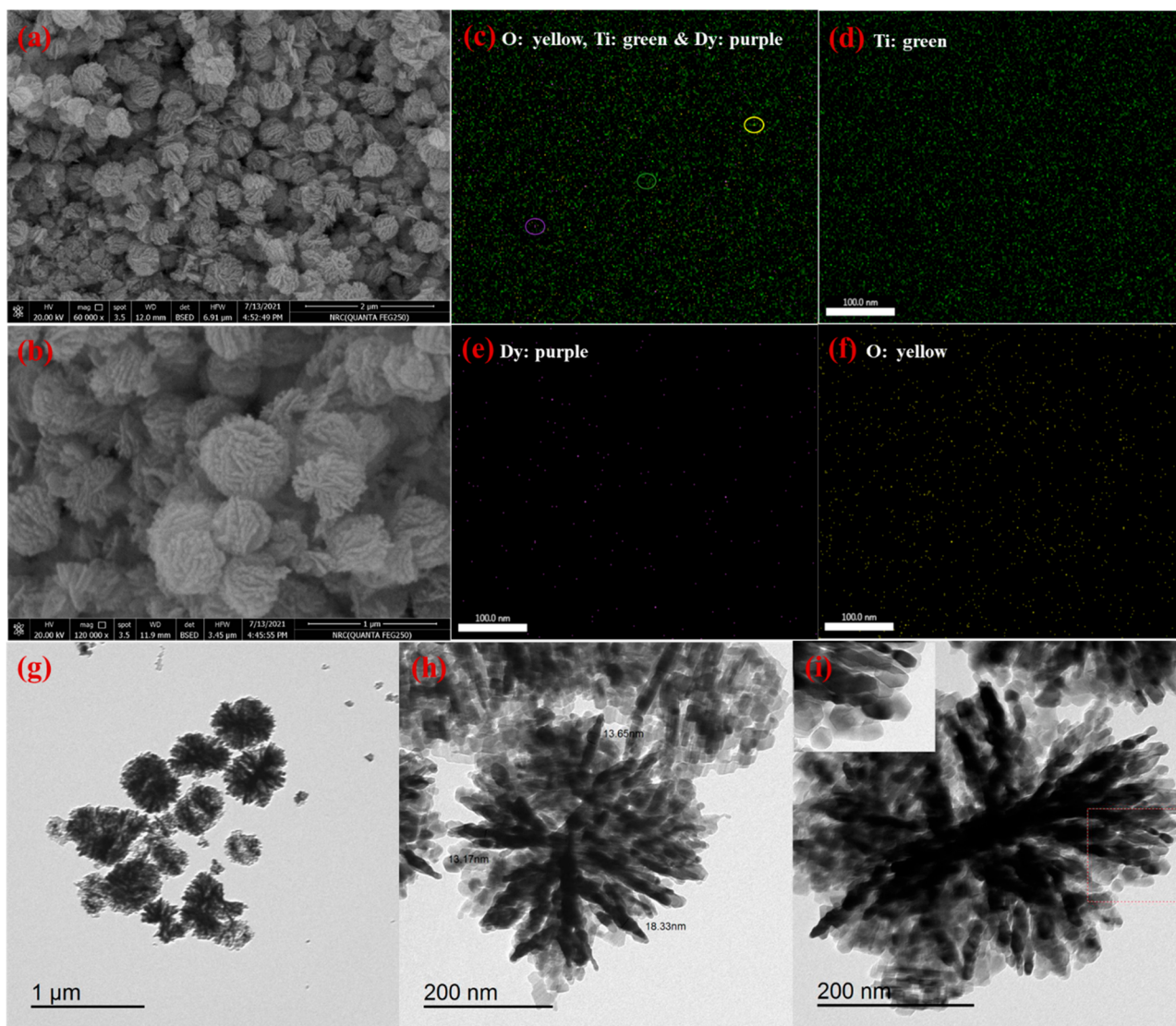
Figure 2. (a, b) SEM, (c−f) EDS-mapping, and (g−i) TEM images of Dy_2O_3/TNF.

discussed later. A Dy_2O_3 separate phase is not readily detected in the XRD patterns of Dy_2O_3/TNF composite due to its smaller particle size or low loading.[40,41] FT-IR spectra of TNF and Dy_2O_3/TNF photocatalysts in the range of 4000−400 cm^{-1} were shown in Figure 1b. The spectrum bands at 498.5, 814.8, 1142.7, 1627.7, and 3431.9 cm^{-1} confirmed the successful preparation of pure anatase nanoflower compared with the previously reported literature.[40−43] The main characteristic observations from the FT-IR spectrum are (1) the absence of acetic acid and acetate bands used in the preparation of TNF after calcination at 700 °C, (2) clear bands below 900 cm^{-1} are related to anatase polymorph, and (3) the presence of surface O−H groups of TiO_2 with stretching mode at ~3500 cm^{-1}. The FT-IR spectrum of Dy_2O_3/TNF is typically identical to that of bare TNF, and both of them reflect the presence of anatase as the main phase of TiO_2.

SEM and TEM images of Dy_2O_3/TNF confirm the nanoflower crystallinity of TiO_2 with ultrafine Dy_2O_3 nanoparticles homogeneously distributed above its surface, as shown in Figures 2 and S1. The spherical hierarchy of the as-prepared photocatalyst consists of a three-dimensional (3D) nanoflower (~0.5 μm) with thin two-dimensional (2D)

nanosheets (~13 nm) that radiate from its center. Moreover, the elemental mapping for 5% Dy_2O_3/TNF photocatalyst (Figure 2c−f) confirms the homogeneity of the catalyst, where Dy_2O_3 nanoparticles are successfully and homogeneously distributed over the TNF surface without any kind of aggregations. The elemental mapping may explain the absence of any diffraction peaks of the Dy_2O_3 phase in the XRD study. The nitrogen adsorption−desorption isotherms as well as the specific surface area (S_{BET}), average pore volume (cc/g), and pore radius DV (r) of TNF and Dy_2O_3/TNF are shown in Figure S2 and summarized in Table S1. The samples exhibit a type II adsorption isotherm with an H3 hysteresis loop, which may be due to some mesoporous nature of the catalysts.[42,43] As shown in Table S1, it was also observed that significant changes in the surface properties after the incorporation of Dy_2O_3, such as the specific surface area, is doubled in the case of the 5% Dy_2O_3/TNF sample compared to that of the TNF sample and then decreased after that, while the average pore volume (cc/g) and pore radius (nm) values remained almost constant at ~0.32 cc/g and 1.62 nm, respectively. These results may also support the fine dispersion of Dy_2O_3 on the TNF surface and inside its pores.
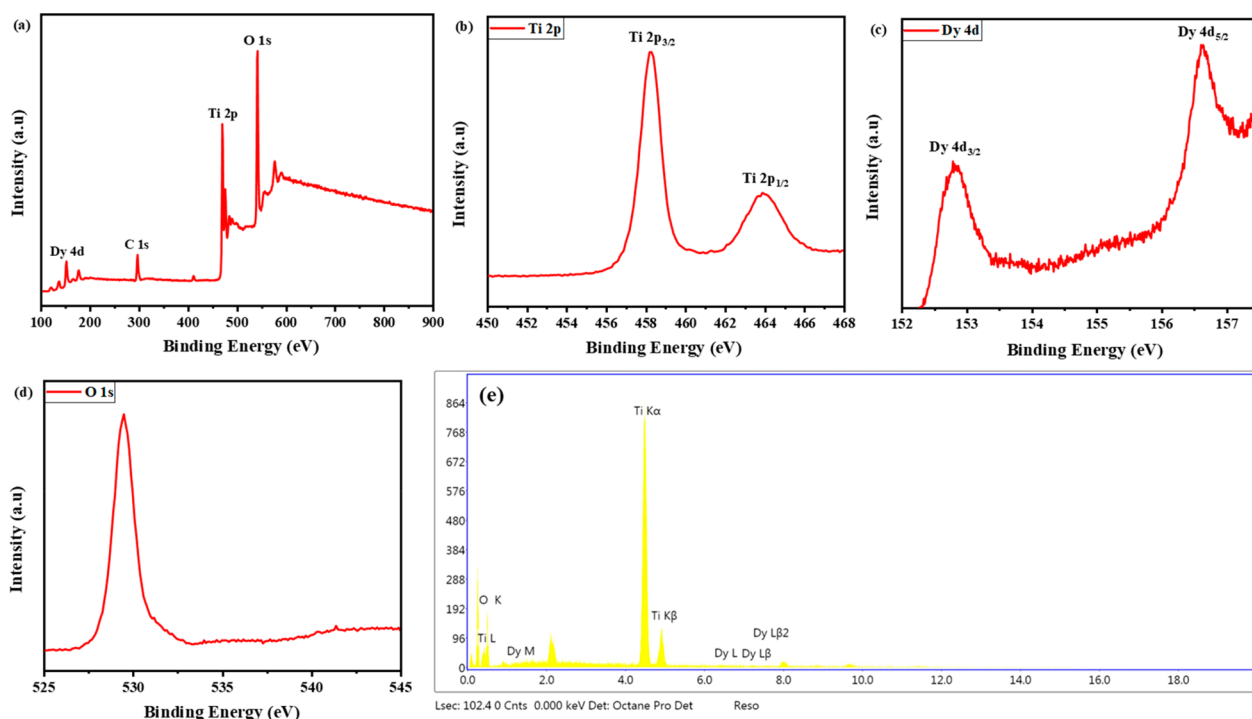
Figure 3. (a–d) XPS and (e) EDS analysis of Dy$_2$O$_3$/TNF.

XPS was applied to probe the bonding and specification environments of titanium, dysprosium, and oxygen in TNF and Dy$_2$O$_3$/TNF photocatalysts (Figure 3a–d). The survey spectrum XPS of Dy$_2$O$_3$/TNF exhibits strong emission lines due to Ti, O, Dy, and a weak C line. The XPS data for high-resolution Ti 2p spectra containing signals at 458.2 and 463.9 eV are in an area ratio of 2:1, respectively. These peaks can be typically attributed to Ti $2p_{1/2}$ and $2p_{3/2}$ levels of Ti(IV) cations.[44] The XPS spectrum of O 1s for Dy$_2$O$_3$/TNF showed a peak at 529.6 eV attributed to the lattice oxygen peak in TiO$_2$ and matching the presence of a surface hydroxyl peak on the FT-IR analysis. The high-resolution XPS for Dy$_2$O$_3$ exhibited two peaks at 152.8 and 156.7 eV attributed to Dy $4d_{3/2}$ and Dy $4d_{5/2}$, respectively.[35,45] The noticed C 1s peak in the survey should be likely due to the acetate organic compound present as traces of carbon on the surface of TNF after thermal treatment at 700 °C. The occupied electrons in Ti $2p_{1/2}$ and $2p_{3/2}$ levels can be readily excited into unoccupied Ti 3d and Ti 3d-O 2p hybrid orbitals. In addition, the excitation of electrons from O 1s to Ti 3d-O 2p hybrid orbitals of TNF.2 energy-dispersive spectroscopy (EDS) shown in Figure 3e reflects the high purity of the prepared sample, and the elemental composition weight ratio was found to be 62:4:34% for titanium, dysprosium, and oxygen, respectively.

The diffuse reflectance UV−vis spectra (DRS) of TNF and different wt % Dy$_2$O$_3$ photocatalysts were used to explore the band gap energy and optical properties (Figure S3). The TNF sample absorbed firmly below 400 nm, concerning the surface defects in TiO$_2$ nanoflower. We note that this absorption is red-shifted, and a new strong edge appeared in the visible wavelengths region after doping with Dy$_2$O$_3$, indicating the visible-light absorption enhancement and potent combination between Dy$_2$O$_3$ and TNF. This observation suggests that Dy$_2$O$_3$/TNF will have better photocatalytic performance than TNF under simulated solar light irradiation. Table S1 summarizes the estimated band gaps for each sample according

to Tauc plots. For TNF, the band gap energy (E_g) was ∼3.24 eV and was typical for the anatase phase.[2] When the loading ratio of Dy$_2$O$_3$ is increased, the band gap drops to 2.95 eV with 5% Dy$_2$O$_3$, as shown in Figure S3.

3.1. Photoelectrochemical Study of TNF and Dy$_2$O$_3$/TNF Photocatalysts. Photocurrent response measurements were used to study the charge-carrier transfer by TNF and Dy$_2$O$_3$/TNF photocatalysts. Figure 4a depicts the transient photocurrent curves (*I-t* plots) at a bias potential of 0 V with several on/off cycles of discontinuous visible-light irradiation. The results obtained under various conditions of darkness and light showed that the photocatalyst could produce the phenomenon of electrons and holes only by exposure to light.[46] The photocurrent response intensity of 5% Dy$_2$O$_3$/TNF was higher than twice that of bare TNF, indicating that the Dy$_2$O$_3$/TNF hybrid can enhance the lifetime of the photogenerated charges compared to the bare TNF. As can be seen in Figure 4b, the photocurrent density observed at the lower bias region for 5% Dy$_2$O$_3$/TNF (0.98 mA/cm^2) was higher regarding that of bare TNF (0.44 mA/cm^2). Such superb enhancement can be assigned to the cocatalytic activity of Dy$_2$O$_3$ played in the nucleophilic attack of oxygen molecules by the electrons transferred from its valence band. The Applied Bias Photon to current conversion Efficiency was estimated for TNF and Dy$_2$O$_3$/TNF at 0 V (vs Ag/AgCl) to be 0.27 and 0.60%, respectively (the applied equation is available in the Experimental Section).[36] The remarkable enhancement in % ABPE of TNF after Dy$_2$O$_3$ is added is attributed to the improvement in the efficient light scattering and charge-transfer properties within the nanoflower morphology.

MS measurements were performed using TNF and Dy$_2$O$_3$/TNF photoanodes at a frequency of 5 kHz and a potential range from −1 to 1.5 V (vs Ag/AgCl) with a scan rate of 50 mV/s. As shown in Figure 4c, the MS plots have a positive slope, reflecting the n-type semiconductivity of both the pristine TNF and Dy$_2$O$_3$/TNF.[38,39] The flat band potential
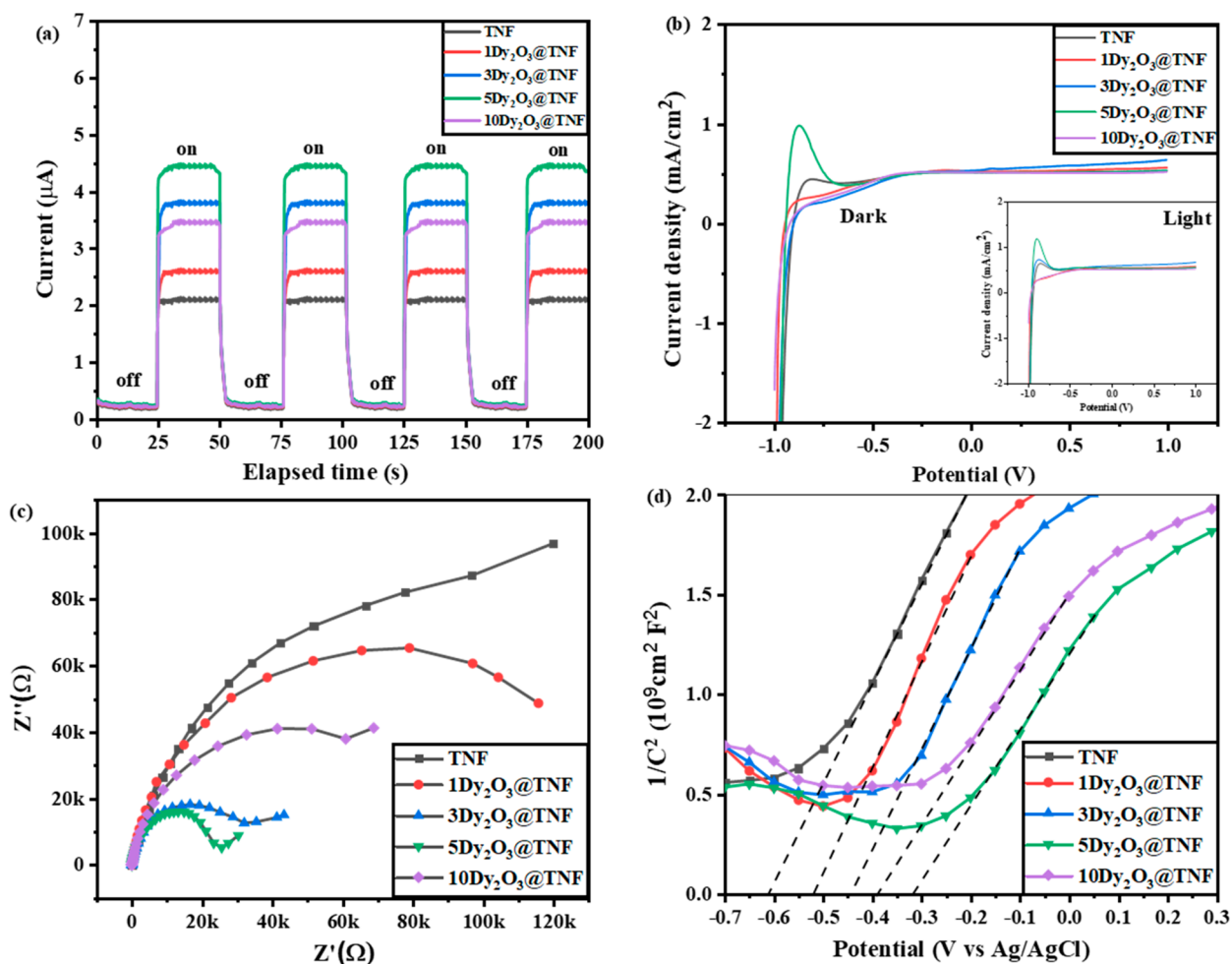
Figure 4. (a) *I-t* and (b) *J-v* curves of as-prepared photocatalysts measured at a bias potential of 0 V vs Ag/AgCl under 1 Sun illumination (100 mW/cm^2) in 0.5 M Na$_2$SO$_4$ solution, (c) MS, and (d) EIS plots.

(E_{FB}) was determined by the intersection of the tangent drawn to the MS plots with the *X*-axis. The flat band potential of 5% Dy$_2$O$_3$/TNF shifted toward the more positive side (E_{FB} = −0.32 ± 0.01 V vs Ag/AgCl) compared to that of bare TNF (E_{FB} = −0.61 ± 0.01 V vs Ag/AgCl). E_{FB} is considered the conduction band in the case of n-type semiconductors, so the valence band of Dy$_2$O$_3$/TNF can be calculated by subtracting the band gap energy to be 2.63 V versus Ag/AgCl. The Fermi level is a hypothetical level below which all the states are occupied, which means that it is always above the valence band. In intrinsic semiconductors, the Fermi level lies exactly in the middle of the VB and CB at absolute zero. However, in extrinsic semiconductors, Fermi levels shift toward the CB in n-type and the VB in p-type. Regarding our extrinsic n-type semiconductors, the positive shift in the Fermi level toward the conduction band after incorporating Dy$_2$O$_3$ within TNF improves the charge transfer density and is compatible with the other results. The Mott−Schottky equation applied to obtain the charge carrier density is available in the Experimental Section.[39,46] Dy$_2$O$_3$/TNF exhibited the carrier density (N_D) of 1.28 × 10^{29}/cm^3, higher than that of bare TNF (0.9383 × 10^{29}/cm^3), supporting the above observation concerning efficient charge transfer/separation and, consequently, enhancement of the photocatalytic performance of Dy$_2$O$_3$/TNF. Moreover, EIS was used to obtain more understanding about the conductivity of the as-prepared

materials, as shown in Figure 4d. Dy$_2$O$_3$/TNF composite has a smaller arc radius regarding TNF photocatalyst and reveals lower charge-transfer resistance on the surface of Dy$_2$O$_3$/TNF compared to TNF.

3.2. Effect of Dy$_2$O$_3$ on the Performance of TNF for the Photo-oxidation of RhB Dye Solution. The photodegradation studies were performed by degrading an aqueous RhB solution using TNF and Dy$_2$O$_3$/TNF at pH 8 under simulated solar light irradiation. As shown in Figure 5a, there was no change in the dye concentration in a control experiment performed in the absence of the photocatalyst, reflecting that RhB dye is resistant to self-photolysis. Before the photocatalytic reaction, TNF and Dy$_2$O$_3$/TNF composites' adsorption performance was investigated over 60 min in RhB dye solution (10 mg L^{-1}) at pH 8 with a photocatalyst weight of 0.4 g L^{-1}. After irradiation for 1 h, the photocatalytic degradation of Dy$_2$O$_3$/TNF composite reached ∼88%, while that of TNF was only 30%. Figure S4 exhibited the absorption spectrum of 10 mg/L RhB dye solution after irradiation for 1 h using a Solar Simulator (100 mW/cm^2) and different photocatalysts. The higher photocatalytic performance of the nanoflower structure, Dy$_2$O$_3$/TNF, compared to the bare TNF can be ascribed to the increase in the visible light absorption and the improved light harvesting due to the reduction in the band gap energy of TNF after the junction with Dy$_2$O$_3$. Furthermore, the influence of Dy$_2$O$_3$ was investigated by
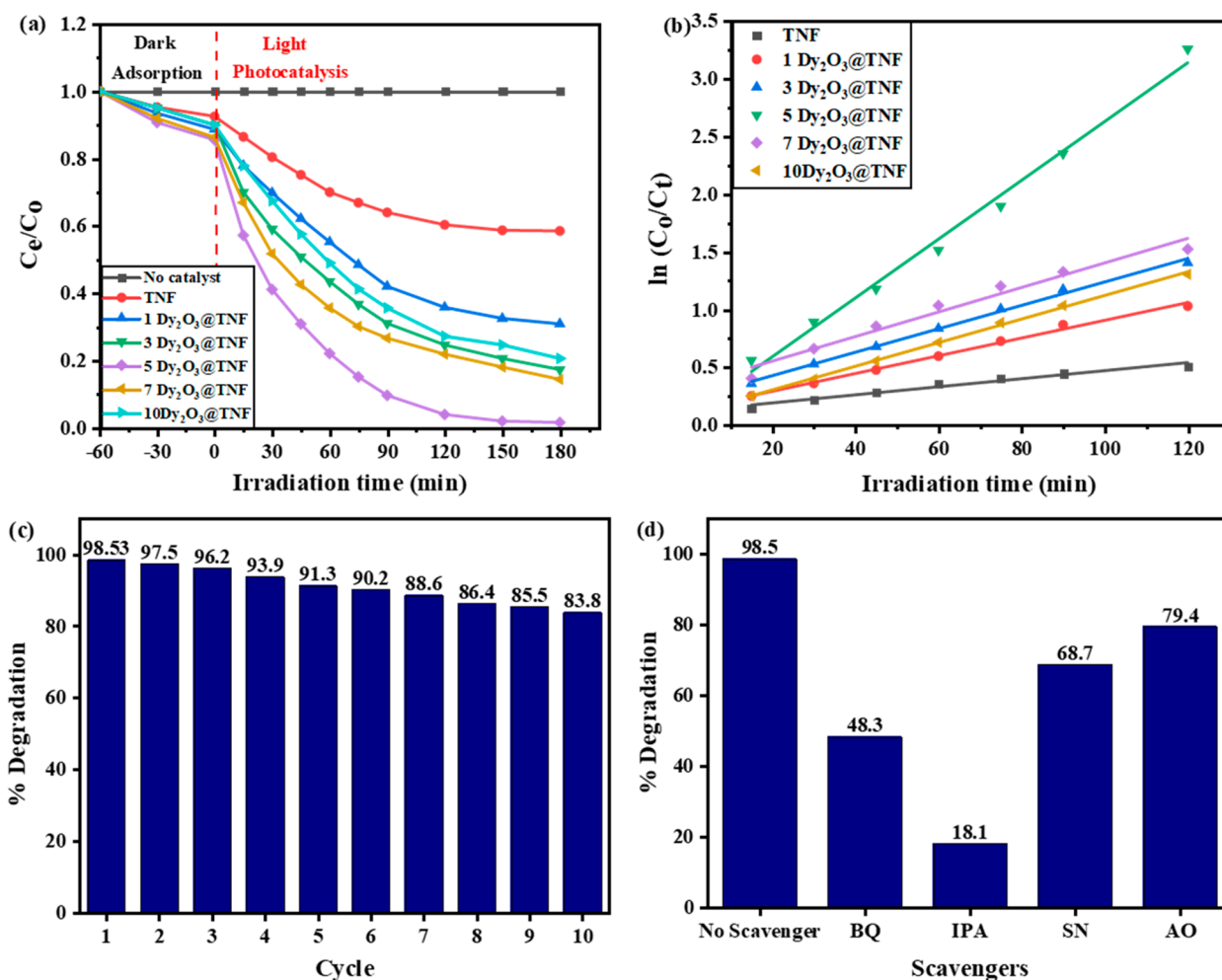
Figure 5. (a) Photocatalytic efficiency, (b) kinetic rates of RhB degradation using TNF and Dy_2O_3/TNF photocatalysts, (c) reusability of Dy_2O_3/TNF for photodegradation of RhB dye, and (d) photocatalytic performance of Dy_2O_3/TNF in the presence of different scavengers.

varying the loading weight percentages in the Dy_2O_3/TNF composite. As shown in Figure 5a, the photodegradation activity of Dy_2O_3/TNF composite increased with increases in the wt % of Dy_2O_3 until it attained the highest efficiency with 5 wt % loading with a sustainable band gap of 2.95 eV.

Generally, the photocatalytic degradation of RhB by irradiated TNF and Dy_2O_3/TNF follows pseudo-first-order kinetics, which is expressed as $kt = \ln(C_o/C_t)$, where C_o is the initial concentration of the dye, C_t is the concentration at time t, and k is the degradation rate constant (min^{-1}).[2,29] Figure 5b shows data for each photocatalyst by plotting $\ln(C_o/C_t)$ versus time with excellent linearity, confirming the perfect applicability of pseudo-first-order kinetics. Among these photocatalysts, 5 wt % Dy_2O_3/TNF exhibits the highest rate constant (k), which is obtained from the slope of the data in Figure 5b and is summarized in Table S1. TNF showed the lowest activity due to the lower excitation energy source than band gap for the sample. The Dy_2O_3/TNF photocatalyst with a rate constant of 0.026 min^{-1} represents one of the highest activities for RhB degradation compared to the previously reported TiO_2-based photocatalyst.[46−54] These results reflect the positive influence of Dy_2O_3 on the photoexcited electron–hole separation in the crystal lattice. The optimum pH and photocatalyst dose for degradation of RhB dye using Dy_2O_3/TNF is shown in Figure S5. The effect of pH on the photodegradation of RhB dye was examined in the pH range of

2−10. After 120 min of irradiation, the percentages of MB degradation at pH 2, 4, 6, 8, and 10 were 37.2, 48.8, 78.5, 95.8, and 98.53%, respectively. The results showed a sharp increase in the removal efficiency of RhB dye with increases in the pH from 2 to 8 followed by a slight increase from pH 8 to 10. Such an adsorption enhancement at the basic medium can be ascribed to the strong electrostatic interaction between the RhB (cationic dye) and the negatively charged surface of the photocatalyst.[56] The chemical stability and reusability of the photocatalyst is a critical issue from an economic point of view. To highlight the stability of Dy_2O_3/TNF, the degradation of fresh RhB dye solutions was repeated for 10 cycles. As shown in Figure 5c, Dy_2O_3/TNF has remarkable photostability and almost maintains the original photocatalytic efficiency, reflecting the leaching resistance of Dy_2O_3/TNF. The reused catalyst was further characterized using an XRD pattern and SEM techniques, as shown in Figure S6. The XRD pattern of the fresh and reused Dy_2O_3/TNF have a similar inline shape and intensity, indicating the successful regeneration of the photocatalyst. SEM also confirmed that the nanoflower topology is retained without destruction. The Dy_2O_3/TNF photocatalyst exhibits good chemical and photostability considering these results.

3.3. Elucidation of Active Species. Irradiation of photocatalysts produces holes in the VB and electrons in the conduction band. Holes undergo an oxidation reaction to
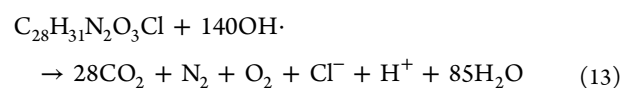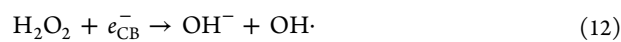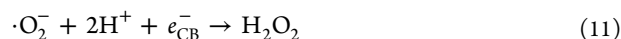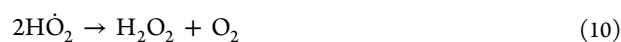
generate hydroxyl radicals (·OH), while electrons react with oxygen in the air through a reduction process to produce superoxide radical anions (·O$_2^-$). Different trapping experiments were performed to investigate the main active species responsible for photodegradation of RhB using Dy$_2$O$_3$/TNF as a photocatalyst. Isopropyl alcohol (IPA), p-benzoquinone (BQ), silver nitrate (SN), and ammonium oxalate (AO) were added to the RhB dye solution as a scavenger for ·OH, ·O$_2^-$, e$^-$, and h$^+$, respectively.[4,55] The photo-oxidation rate of RhB dye (10 mg/L) after 120 min of irradiation without the addition of any capture reagent was 98.5%, while by additions of IPA, BQ, SN, and AO this rate was 18.1, 48.3, 68.7, and 79.4%, respectively (Figure 5d). According to these results, ·OH and ·O$_2^-$ play the most significant influence on the photodegradation of RhB, while h$^+$ and e$^-$ have a secondary role in the degradation of RhB using Dy$_2$O$_3$/TNF as photocatalyst.

3.4. Mechanism of Degradation.

The schematic proposed photodegradation mechanism of our wastewater treatment photocatalyst is shown below and includes four steps: (1) absorption of visible light by photocatalyst generates holes in the valence band and e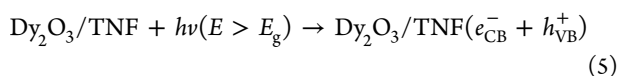lectrons in the conduction band. (2) Holes undergo an oxidation reaction to generate hydroxyl radicals (·OH). (3) Electrons react with oxygen in the air through a reduction process to produce superoxide radical anions (·O$_2^-$), then H$_2$O$_2$, and finally ·OH. (4) The generated active radicals degrade the organic pollutants to produce harmless molecules (H$_2$O and CO$_2$). Scheme 1 and

Scheme 1. Proposed Photodegradation Mechanism of RhB Wastewater Treatment Using Dy$_2$O$_3$/TNF Photocatalyst
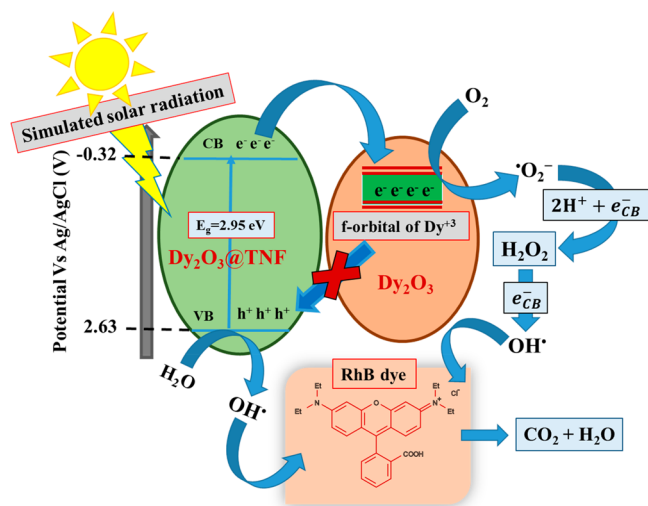
eqs 5−13 describe the formation of active radicals using Dy$_2$O$_3$/TNF under simulated solar light irradiation.[2,34,54]

$$Dy_2O_3/TNF + h\nu(E > E_g) \rightarrow Dy_2O_3/TNF(e_{CB}^- + h_{VB}^+) \quad (5)$$

$$H_2O + h_{VB}^+ \rightarrow H^+ + OH\cdot \quad (6)$$

$$OH^- + h_{VB}^+ \rightarrow OH\cdot \quad (7)$$

$$O_2 + e_{CB}^- \rightarrow \dot{O}_2^- \quad (8)$$

$$\cdot O_2^- + H^+ \rightarrow H\dot{O}_2 \quad (9)$$

$$2H\dot{O}_2 \rightarrow H_2O_2 + O_2 \quad (10)$$

$$\cdot O_2^- + 2H^+ + e_{CB}^- \rightarrow H_2O_2 \quad (11)$$

$$H_2O_2 + e_{CB}^- \rightarrow OH^- + OH\cdot \quad (12)$$

$$C_{28}H_{31}N_2O_3Cl + 140OH\cdot$$
$$\rightarrow 28CO_2 + N_2 + O_2 + Cl^- + H^+ + 85H_2O \quad (13)$$

3.5. Comparison of Dy$_2$O$_3$/TNF with the Previously Reported Photocatalysts.

To elucidate the catalyst efficiency, the photodegradation of RhB dye using different photocatalysts previously reported in the literature is recorded in Table 1. A comparison study includes the photocatalyst

Table 1. Comparison Study for Degradation of RhB Dye in the Presence of Dy$_2$O$_3$/TNF with Other Photocatalysts Reported in the Literature

photocatalyst	light source	dosage (g/L)	reaction time (min)	removal efficiency	ref
Dy$_2$O$_3$/TNF	Solar Simulator, 100 mW	0.4	120	98.5%	this work
Bi$_2$O$_3$/g-C$_3$N$_4$	Hg−Xe lamp, 15 mW	0.3	180	83.0%	57
P25	two lead NULITE, 50 W	1.0	180	78.6%	58
g-C$_3$N$_4$/Ag/Ag$_3$VO$_4$	xenon lamp, 250 W	1.0	105	62.9%	59
commercial TiO$_2$	xenon lamp, 350 W	1.5	75	30.0%	60
ZnO-rGO	UV	0.4	120	92.0%	61

dosage, reaction contact time, and light source. Considering the literature values, Dy$_2$O$_3$/TNF reached satisfactory results in photocatalytic degradation of RhB dye.

4. CONCLUSION

In conclusion, the developed photocatalyst has a highly crystalline morphology with a hierarchical nanoflower structure of TiO$_2$ doped with a nanosized Dy$_2$O$_3$. The photocatalytic activity of Dy$_2$O$_3$/TNF was investigated by the photo-oxidation of aqueous rhodamine B solution under simulated solar light irradiation. The enhanced visible-light absorption of Dy$_2$O$_3$/TNF is attributed to the f-f trasitions present in the f-orbitals of Dy$_2$O$_3$. Upon irradiation of Dy$_2$O$_3$/TNF with visible light, the electrons in the TNF valence band outer shell are excited to the conduction band and are finally trapped in the f-shell of Dy$_2$O$_3$. Hence, the superior performance of Dy$_2$O$_3$/TNF is aroused from its acceptable band gap, enhanced charge transfer, improvement of charge separation, and high photogenerated charge stability. Additionally, the excellent chemical stability of the catalyst facilitates its separation from the dye solution and is recycled without any significant loss of photocatalytic efficiency. Notably, the photoelectrochemical properties and photo-oxidation mechanism of the Dy$_2$O$_3$/TNF photocatalyst are thoroughly revealed by several techniques, providing outstanding opportunities for the design of high-performance and cost-effective photocatalysts.

■ ASSOCIATED CONTENT

ⓢ Supporting Information

The Supporting Information is available free of charge at https://pubs.acs.org/doi/10.1021/acsomega.2c01090.

> SEM images of TNF, 3% Dy_2O_3/TNF, 5% Dy_2O_3/TNF, and 10% Dy_2O_3/TNF. TEM images of Dy_2O_3/TNF. N_2 adsorption−desorption isotherms of the as-synthesized materials. UV−Vis diffuse reflectance spectroscopy and the intrinsic band gap (Tauc plot) of the as-synthesized samples. Absorption spectrum of 10 mg/L RhB dye solution after irradiation for 1 h using Solar Simulator (100 mW/cm^2) and different photocatalysts. Effect of initial pH and catalyst dose on the performance of Dy_2O_3/TNF photocatalyst for degradation of RhB dye. XRD pattern and SEM image of 5% Dy_2O_3/TNF photocatlyst after reusability for 10 cycles of RhB solution photodegradation. Summarized structural, physical, and photocatalytic data for TNF and Dy_2O_3/TNF photocatalysts (PDF)

■ AUTHOR INFORMATION

Corresponding Authors

Abdelrahman S. Khder − *Department of Chemistry, Faculty of Science, Mansoura University, 35516 Mansoura, Egypt; Chemistry Department, Faculty of Applied Science, Umm Al-Qura University, 21955 Makkah, Saudi Arabia;* ⓞ orcid.org/0000-0002-4886-6116; Email: askhder@uqu.edu.sa, askhder2244@yahoo.com

Saleh A. Ahmed − *Chemistry Department, Faculty of Applied Science, Umm Al-Qura University, 21955 Makkah, Saudi Arabia; Chemistry Department, Faculty of Science, Assiut University, 71516 Assiut, Egypt;* ⓞ orcid.org/0000-0002-2364-0380; Email: saahmed@uqu.edu.sa, saleh_63@hotmail.com

Awad I. Ahmed − *Department of Chemistry, Faculty of Science, Mansoura University, 35516 Mansoura, Egypt;* Email: awahmed@mans.edu.eg

Authors

Mahmoud M. Kaid − *Department of Chemistry, Faculty of Science, Mansoura University, 35516 Mansoura, Egypt*

Amr A. Ibrahim − *Department of Chemistry, Faculty of Science, Mansoura University, 35516 Mansoura, Egypt*

Hatem M. Altass − *Chemistry Department, Faculty of Applied Science, Umm Al-Qura University, 21955 Makkah, Saudi Arabia*

Reem I. Alsantali − *Department of Pharmaceutical Chemistry, College of Pharmacy, Taif University, 21944 Taif, Saudi Arabia*

Rabab S. Jassas − *Department of Chemistry, Jamoum University College, Umm Al-Qura University, 21955 Makkah, Saudi Arabia*

Menna A. Khder − *Department of Chemistry, Faculty of Science, Mansoura University, 35516 Mansoura, Egypt*

Munirah M. Al-Rooqi − *Chemistry Department, Faculty of Applied Science, Umm Al-Qura University, 21955 Makkah, Saudi Arabia*

Ziad Moussa − *Department of Chemistry, College of Science, United Arab Emirates University, 15551 Al Ain, Abu Dhabi, United Arab Emirates;* ⓞ orcid.org/0000-0002-3365-0451

Complete contact information is available at:
https://pubs.acs.org/10.1021/acsomega.2c01090

Author Contributions

M.M.K.: Methodology, Data curation, Validation, Investigation and Writing-Reviewing the manuscript draft preparation; A.S.K.: Conceptualization, Methodology, Data curation, Validation, Investigation, Visualization, S.A.A.: Main idea, Conceptualization, Methodology, Data curation, Validation, Investigation, Visualization, Project administration, Supervision, Funding acquisition, Writing-Reviewing and Editing the manuscript; A.A.I.: Validation, Data curation and Investigation, H.M.A.: Validation, Data curation and Investigation, R.I.A.: Validation, Data curation and Investigation and Funding acquisition, R.S.J.: Methodology, Data curation, Validation, Investigation and Funding acquisition; M.A.K.: Validation, Data curation and Investigation, M.M.A.-R.: Methodology, Data curation, Validation, Investigation and Funding acquisition, Z.M.: Data curation, Validation, Funding acquisition, Visualization and Editing the manuscript, A.I.A.: Validation Visualization and first draft preparation.

Notes

The authors declare no competing financial interest.

■ ACKNOWLEDGMENTS

■ REFERENCES

(1) Xu, J.; Zheng, X.; Feng, Z.; Lu, Z.; Zhang, Z.; Huang, W.; Li, Y.; Vuckovic, D.; Li, Y.; Dai, S.; Chen, G.; Wang, K.; Wang, H.; Chen, J. K.; Mitch, W.; Cui, Y. Organic Wastewater Treatment by a Single-Atom Catalyst and Electrolytically Produced H_2O_2. *Nat. Sustain.* **2021**, *4* (3), 233−241.

(2) Harris, J.; Silk, R.; Smith, M.; Dong, Y.; Chen, W. T.; Waterhouse, G. I. N. Hierarchical TiO2Nanoflower Photocatalysts with Remarkable Activity for Aqueous Methylene Blue Photo-Oxidation. *ACS Omega* **2020**, *5* (30), 18919−18934.

(3) Al-Mamun, M. R.; Kader, S.; Islam, M. S.; Khan, M. Z. H. Photocatalytic Activity Improvement and Application of UV-TiO2 Photocatalysis in Textile Wastewater Treatment: A Review. *J. Environ. Chem. Eng.* **2019**, *7* (5), 103248.

(4) Anwer, H.; Mahmood, A.; Lee, J.; Kim, K. H.; Park, J. W.; Yip, A. C. K. Photocatalysts for Degradation of Dyes in Industrial Effluents: Opportunities and Challenges. *Nano Res.* **2019**, *12*, 955−972.

(5) Rueda-Marquez, J. J.; Levchuk, I.; Fernández Ibañez, P.; Sillanpää, M. A. Critical Review on Application of Photocatalysis for Toxicity Reduction of Real Wastewaters. *J. Clean. Prod.* **2020**, *258*, 120694.

(6) Kaid, M. M.; Gebreil, A.; El-Hakam, S. A.; Ahmed, A. I.; Ibrahim, A. A. Sulfamic Acid Incorporated HKUST-1: A Highly Active Catalyst and Efficient Adsorbent. *RSC Adv.* **2020**, *10* (26), 15586−15597.

(7) Hodges, B. C.; Cates, E. L.; Kim, J. H. Challenges and Prospects of Advanced Oxidation Water Treatment Processes Using Catalytic Nanomaterials. *Nat. Nanotechnol.* **2018**, *13* (8), 642−650.

(8) Miklos, D. B.; Remy, C.; Jekel, M.; Linden, K. G.; Drewes, J. E.; Hübner, U. Evaluation of Advanced Oxidation Processes for Water and Wastewater Treatment − A Critical Review. *Water Res.* **2018**, *139*, 118−131.

(9) Lyu, L.; Zhang, L.; Wang, Q.; Nie, Y.; Hu, C. Enhanced Fenton Catalytic Efficiency of γ-Cu-Al2O3 by σ-Cu2+-Ligand Complexes from Aromatic Pollutant Degradation. *Environ. Sci. Technol.* **2015**, *49* (14), 8639−8647.

(10) Pham, A. L. T.; Lee, C.; Doyle, F. M.; Sedlak, D. L. A Silica-Supported Iron Oxide Catalyst Capable of Activating Hydrogen Peroxide at Neutral PH Values. *Environ. Sci. Technol.* **2009**, *43* (23), 8930−8935.

(11) Costa, R. C. C.; Lelis, M. F. F.; Oliveira, L. C. A.; Fabris, J. D.; Ardisson, J. D.; Rios, R. R. V. A.; Silva, C. N.; Lago, R. M. Novel Active Heterogeneous Fenton System Based on Fe3-XM XO4 (Fe, Co, Mn, Ni): The Role of M^{2+} Species on the Reactivity towards H_2O_2 Reactions. *J. Hazard. Mater.* **2006**, *129* (1−3), 171−178.

(12) Neyens, E.; Baeyens, J. A Review of Classic Fenton's Peroxidation as an Advanced Oxidation Technique. *J. Hazard. Mater.* **2003**, *98* (1−3), 33−50.

(13) Li, S.; Wang, C.; Cai, M.; Yang, F.; Liu, Y.; Chen, J.; Zhang, P.; Li, X.; Chen, X. Facile Fabrication of TaON/Bi2MoO6 Core−Shell S-Scheme Heterojunction Nanofibers for Boosting Visible-Light Catalytic Levofloxacin Degradation and Cr(VI) Reduction. *Chem. Eng.* **2022**, *428*, 131158.

(14) Thirumalai, K.; Balachandran, S.; Shanthi, M.; Swaminathan, M. Heterostructured Dysprosium Vanadate − ZnO for Photo-Electrocatalytic and Self-Cleaning Applications. *Mater. Sci. Semicond. Process.* **2017**, *71*, 84−92.

(15) Muruganandham, M.; Suri, R. P. S.; Sillanpää, M.; Wu, J. J.; Ahmmad, B.; Balachandran, S.; Swaminathan, M. Recent Developments in Heterogeneous Catalyzed Environmental Remediation Processes. *J. Nanosci. Nanotechnol.* **2014**, *14*, 1898−1910.

(16) Liu, X.; Gu, S.; Zhao, Y.; Zhou, G.; Li, W. BiVO4, Bi_2WO_6 and Bi_2MoO_6 Photocatalysis: A Brief Review. *J. Mater. Sci. Technol.* **2020**, *56*, 45−68.

(17) Liu, J.; Hodes, G.; Yan, J.; Liu, S. (Frank). Metal-Doped Mo2C (Metal = Fe, Co, Ni, Cu) as Catalysts on TiO2 for Photocatalytic Hydrogen Evolution in Neutral Solution. *Chin. J. Catal.* **2021**, *42* (1), 205−216.

(18) Thirumalai, K.; Shanthi, M.; Swaminathan, M. Hydrothermal Fabrication of Natural Sun Light Active Dy_2WO_6 Doped ZnO and Its Enhanced Photo-Electrocatalytic Activity and Self-Cleaning Properties. *RSC Adv.* **2017**, *7* (13), 7509−7518.

(19) Zuo, G.; Wang, Y.; Teo, W. L.; Xian, Q.; Zhao, Y. Direct Z-Scheme TiO_2−$ZnIn_2S_4$ Nanoflowers for Cocatalyst-Free Photocatalytic Water Splitting. *Appl. Catal., B* **2021**, *291*, 120126.

(20) Luo, Y.-N.; Li, Y.; Qian, L.-l.; Wang, X.-T.; Wang, J.; Wang, C.-W. Excellent Photocatalytic Performance from NiS Decorated TiO2 Nanoflowers with Exposed {001} Facets. *Mater. Res. Bull.* **2020**, *130*, 110945.

(21) Wang, Y.; Zhang, M.; Lv, S.; Li, X.; Wang, D.; Song, C. Photogenerated Oxygen Vacancies in Hierarchical Ag/TiO2Nanoflowers for Enhanced Photocatalytic Reactions. *ACS Omega* **2020**, *5* (23), 13994−14005.

(22) Kunwar, S.; Pandit, S.; Kulkarni, R.; Mandavkar, R.; Lin, S.; Li, M. Y.; Lee, J. Hybrid Device Architecture Using Plasmonic Nanoparticles, Graphene Quantum Dots, and Titanium Dioxide for UV Photodetectors. *ACS Appl. Mater. Interfaces.* **2021**, *13* (2), 3408−3418.

(23) Lin, J. X.; Thaomonpun, J.; Thongpool, V.; Chen, W. J.; Huang, C. H.; Sun, S. J.; Remes, Z.; Tseng, Y. T.; Liao, Y. F.; Hsu, H. S. Enhanced Photodegradation in Metal Oxide Nanowires with Co-Doped Surfaces under a Low Magnetic Field. *ACS Appl. Mater. Interfaces.* **2021**, *13* (19), 23173−23180.

(24) Rubino, A.; Zanoni, R.; Schiavi, P. G.; Latini, A.; Pagnanelli, F. Two-Dimensional Restructuring of Cu2O Can Improve the Performance of Nanosized n-TiO2/p-Cu2O Photoelectrodes under UV-Visible Light. *ACS Appl. Mater. Interfaces.* **2021**, *13* (40), 47932−47944.

(25) G A, S. J.; Arumugam, S. Rare-Earth-Based MIS Type Core−Shell Nanospheres with Visible-Light-Driven Photocatalytic Activity

(26) Bak, T.; Nowotny, J.; Rekas, M.; Sorrell, C. C. Photo-Electrochemical Hydrogen Generation from Water Using Solar Energy. Materials-Related Aspects. *Int. J. Hydrog. Energy* **2002**, *27*, 991−1022.

(27) Chen, W. T.; Dosado, A. G.; Chan, A.; Sun-Waterhouse, D.; Waterhouse, G. I. N. Highly Reactive Anatase Nanorod Photocatalysts Synthesized by Calcination of Hydrogen Titanate Nanotubes: Effect of Calcination Conditions on Photocatalytic Performance for Aqueous Dye Degradation and H2 Production in Alcohol-Water Mixtures. *Appl. Catal. A: Gen.* **2018**, *565*, 98−118.

(28) Chen, W. T.; Chan, A.; Jovic, V.; Sun-Waterhouse, D.; Murai, K. I.; Idriss, H.; Waterhouse, G. I. N. Effect of the TiO2 Crystallite Size, TiO2 Polymorph and Test Conditions on the Photo-Oxidation Rate of Aqueous Methylene Blue. *Top Catal.* **2015**, *58* (2−3), 85−102.

(29) Lui, G.; Liao, J. Y.; Duan, A.; Zhang, Z.; Fowler, M.; Yu, A. Graphene-Wrapped Hierarchical TiO2 Nanoflower Composites with Enhanced Photocatalytic Performance. *J. Mater. Chem.* **2013**, *1* (39), 12255−12262.

(30) Guo, D.; Feng, D.; Zhang, Y.; Zhang, Z.; Wu, J.; Zhao, Y.; Sun, S. (2022). Synergistic mechanism of biochar-nano TiO2 adsorption-photocatalytic oxidation of toluene. *Fuel Process. Technol.* **2022**, *229*, 107200.

(31) Li, C.; Sun, T.; Zhang, D.; Zhang, X.; Qian, Y.; Zhang, Y.; Lin, X.; Liu, J.; Zhu, L.; Wang, X.; Shi, Z.; Lin, Q. Fabrication of ternary Ag/La-black TiO_2-x photocatalyst with enhanced visible-light photocatalytic activity for tetracycline degradation. *J. Alloys Compd.* **2022**, *891*, 161960.

(32) Liao, J.-Y.; He, J.-W.; Xu, H.; Kuang, D.-B.; Su, C.-Y. Effect of TiO2 Morphology on Photovoltaic Performance of Dye-Sensitized Solar Cells: Nanoparticles, Nanofibers, Hierarchical Spheres and Ellipsoid Spheres. *J. Mater. Chem.* **2012**, *22* (16), 7910−7918.

(33) Josephine, G. A. S.; Sivasamy, A. Nanocrystalline ZnO Doped Dy2O3 a Highly Active Visible Photocatalyst: The Role of Characteristic f Orbital's of Lanthanides for Visible Photoactivity. *Appl. Catal., B* **2014**, *150−151*, 288−297.

(34) Sheydaei, M.; Soleimani, D.; Ayoubi-Feiz, B. Simultaneous Immobilization of Dy2O3, Graphite and TiO2 to Prepare Stable Nanocomposite for Visible Light Assisted Photocatalytic Ozonation of a Wastewater: Modeling via Artificial Neural Network. *Environ. Technol. Innov.* **2020**, *17*, 355−363.

(35) Yein, W. T.; Wang, Q.; Feng, X.; Li, Y.; Wu, X. Enhancement of Photocatalytic Performance in Sonochemical Synthesized ZnO−RGO Nanocomposites Owing to Effective Interfacial Interaction. *Environ. Chem. Lett.* **2018**, *16* (1), 251−264.

(36) Zhang, S.; Chen, D.; Liu, Z.; Ruan, M.; Guo, Z. Novel Strategy for Efficient Water Splitting through Pyro-Electric and Pyro-Photo-Electric Catalysis of BaTiO3 by Using Thermal Resource and Solar Energy. *Appl. Catal., B* **2021**, *284*, 119686.

(37) Salem, K. E.; Mokhtar, A. M.; Soliman, I.; Ramadan, M.; Shaheen, B. S.; Allam, N. K. Ge-Doped ZnO Nanorods Grown on FTO for Photoelectrochemical Water Splitting with Exceptional Photoconversion Efficiency. *Int. J. Hydrog. Energy* **2021**, *46* (1), 209−220.

(38) Tayebi, M.; Tayyebi, A.; Masoumi, Z.; Lee, B. K. Photo-corrosion Suppression and Photoelectrochemical (PEC) Enhancement of ZnO via Hybridization with Graphene Nanosheets. *Appl. Surf. Sci.* **2020**, *502*, 144189.

(39) McCarthy, D. N.; Risse, S.; Katekomol, P.; Kofod, G. The Effect of Dispersion on the Increased Relative Permittivity of TiO 2/ SEBS Composites. *J. Phys. D: Appl. Phys.* **2009**, *42* (14), 145406.

(40) Nolan, N. T.; Seery, M. K.; Pillai, S. C. Spectroscopic Investigation of the Anatase-to-Rutile Transformation of Sol-Gel-Synthesized TiO2 Photocatalysts. *J. Phys. Chem. C* **2009**, *113* (36), 16151−16157.

through an Electron Hopping−trapping Mechanism. *ACS Omega* **2018**, *3* (1), 1090−1101.

(41) Saud, H. R.; Al-Taweel, S. S. New Route for Synthesis of Pure Anatase TiO₂ Nanoparticles via Ultrasound-Assisted Sol-Gel Method. *J. Chem. Pharm.* **2016**, *8* (2), 620−626.

(42) Green, I. X.; Tang, W.; Neurock, M.; Yates, J. T. Mechanistic Insights into the Partial Oxidation of Acetic Acid by O₂ at the Dual Perimeter Sites of a Au/TiO₂ Catalyst. *Faraday Discuss.* **2013**, *162*, 247−265.

(43) Liao, L. F.; Lien, C. F.; Lin, J. L. FTIR Study of Adsorption and Photoreactions of Acetic Acid on TiO2. *Phys. Chem. Chem. Phys.* **2001**, *3* (17), 3831−3837.

(44) Cai, Q.; Li, X.; Hu, E.; Wang, Z.; Lv, P.; Zheng, J.; Yu, K.; Wei, W.; Ostrikov, K. Overcoming Ion Transport Barrier by Plasma Heterointerface Engineering: Epitaxial Titanium Carbonitride on Nitrogen-Doped TiO2 for High-Performance Sodium-Ion Batteries. *Small* **2022**, *18*, 2200694.

(45) Gopinath, K.; Chinnadurai, M.; Devi, N. P.; Bhakyaraj, K.; Kumaraguru, S.; Baranisri, T.; Sudha, A.; Zeeshan, M.; Arumugam, A.; Govindarajan, M.; Alharbi, N. S.; Kadaikunnan, S.; Benelli, G. One-Pot Synthesis of Dysprosium Oxide Nano-Sheets: Antimicrobial Potential and Cyotoxicity on A549 Lung Cancer Cells. *J. Clust. Sci.* **2017**, *28* (1), 621−635.

(46) Kumar, S.; Kaushik, R. D.; Upadhyay, G. K.; Purohit, L. P. RGO-ZnO Nanocomposites as Efficient Photocatalyst for Degradation of 4-BP and DEP Using High Temperature Refluxing Method in in-Situ Condition. *J. Hazard. Mater.* **2021**, *406*, 124300.

(47) Mou, H.; Song, C.; Zhou, Y.; Zhang, B.; Wang, D. Design and Synthesis of Porous Ag/ZnO Nanosheets Assemblies as Super Photocatalysts for Enhanced Visible-Light Degradation of 4-Nitrophenol and Hydrogen Evolution. *Appl. Catal., B* **2018**, *221*, 565−573.

(48) Mu, J.; Luo, D.; Miao, H.; Fan, J.; Hu, X. Synergistic Wide Spectrum Response and Directional Carrier Transportation Characteristics of Se/SnSe₂/TiO₂ Multiple Heterojunction for Efficient Photoelectrochemical Simultaneous Degradation of Cr (VI) and RhB. *Appl. Surf. Sci.* **2021**, *542*, 148673.

(49) Yang, H.; Zheng, F.; Liu, F.; Lin, L.; Huang, X.; Lin, Y.; Li, S. Positively and Negatively Charged Double Shell with Au Sandwich for Protecting and Enhancing Photocatalytic Activity of TiO₂-Based Photocatalyst. *J. Phys. Chem.* **2021**, *125* (43), 23729−23735.

(50) Zhuang, J.; Dai, W.; Tian, Q.; Li, Z.; Xie, L.; Wang, J.; Liu, P.; Shi, X.; Wang, D. Photocatalytic Degradation of RhB over TiO2 Bilayer Films: Effect of Defects and Their Location. *Langmuir* **2010**, *26* (12), 9686−9694.

(51) Gao, Y.; Wang, T. Preparation of Ag₂O/TiO₂ Nanocomposites by Two-Step Method and Study of Its Degradation of RHB. *J. Mol. Struct.* **2021**, *1224*, 129049.

(52) Zhang, L.; He, Y.; Wu, Y.; Wu, T. Photocatalytic Degradation of RhB over MgFe2O 4/TiO2 Composite Materials. *Mater. Sci. Eng. B: Solid-State Mater. Adv. Technol.* **2011**, *176* (18), 1497−1504.

(53) Wang, J.; Wang, G.; Wei, X.; Liu, G.; Li, J. ZnO Nanoparticles Implanted in TiO 2 Macrochannels as an Effective Direct Z-Scheme Heterojunction Photocatalyst for Degradation of RhB. *Appl. Surf. Sci.* **2018**, *456*, 666−675.

(54) Xu, C.; Yang, F.; Deng, B.; Che, S.; Yang, W.; Zhang, G.; Sun, Y.; Li, Y. RGO-Wrapped Ti3C2/TiO2 Nanowires as a Highly Efficient Photocatalyst for Simultaneous Reduction of Cr(VI) and Degradation of RhB under Visible Light Irradiation. *J. Alloys Compd.* **2021**, *874*, 159865.

(55) Chu, C.-Y.; Huang, M. H. Facet-dependent photocatalytic properties of Cu2O crystals probed by using electron, hole and radical scavengers. *J. Mater. Chem. A* **2017**, *5*, 15116−15123.

(56) Ribao, P.; Corredor, J.; Rivero, M. J.; Ortiz, I. Role of Reactive Oxygen Species on the Activity of Noble Metal-Doped TiO2 Photocatalysts. *J. Hazard. Mater.* **2019**, *372*, 45−51.

(57) Ben Abdelaziz, M.; Chouchene, B.; Balan, L.; Gries, T.; Medjahdi, G.; Ezzaouia, H.; Schneider, R. One Pot Synthesis of Bismuth Oxide/Graphitic Carbon Nitride Composites with High Photocatalytic Activity. *Mol. Catal.* **2019**, *463*, 110−118.

(58) Phongamwong, T.; Donphai, W.; Prasitchoke, P.; Rameshan, C.; Barrabés, N.; Klysubun, W.; Rupprechter, G.; Chareonpanich, M. Novel Visible-Light-Sensitized Chl-Mg/P25 Catalysts for Photocatalytic Degradation of Rhodamine B. *Appl. Catal., B* **2017**, *207*, 326−334.

(59) Wu, J.; Shen, X.; Miao, X.; Ji, Z.; Wang, J.; Wang, T.; Liu, M. An All-Solid-State Z-Scheme g-C3N4/Ag/Ag3VO4 Photocatalyst with Enhanced Visible-Light Photocatalytic Performance. *Eur. J. Inorg. Chem.* **2017**, *2017* (21), 2845−2853.

(60) Bai, S.; Liu, H.; Sun, J.; Tian, Y.; Chen, S.; Song, J.; Luo, R.; Li, D.; Chen, A.; Liu, C. C. Improvement of TiO₂ Photocatalytic Properties under Visible Light by WO₃ /TiO₂ and MoO₃ /TiO₂ Composites. *Appl. Surf. Sci.* **2015**, *338*, 61−68.

(61) Zhao, Y.; Liu, L.; Cui, T.; Tong, G.; Wu, W. Enhanced photocatalytic properties of ZnO/reduced grapheneoxide sheets (rGO) composites with controllable morphology and composition. *Appl. Surf. Sci.* **2017**, *412*, 58−68.